Effect of sequential N ion implantation in the formation of a shallow Mg-implanted *p*-type GaN layer

Jun Uzuhashi[1,2*], Jun Chen[1*], Ryo Tanaka[3], Shinya Takashima[3], Masaharu Edo[3], Tadakatsu Ohkubo[1], and Takashi Sekiguchi[1,2]

[1]*National Institute for Materials Science, Tsukuba, 305-0047, Japan*
[2]*University of Tsukuba, Tsukuba 305-8577, Japan*
[3]*Advanced Technology Laboratory, Fuji Electric Co., Ltd., Hino, Tokyo 191-8502, Japan*

[*] Authors to whom correspondence should be addressed:
UZUHASHI.Jun@nims.go.jp and CHEN.Jun@nims.go.jp

Keywords: gallium nitride, ion implantation, transmission electron microscopy, atom probe tomography, cathodoluminescence

Abstract

An area-selectable Mg doping via ion implantation (I/I) is essential to realize gallium nitride (GaN) based power switching devices. Conventional post-implantation annealing forms considerable defects in the GaN, resulting in extremely low activation efficiency. The recent invention of ultra-high-pressure annealing (UHPA) has substantially improved the *p*-type activation efficiency, however, the UHPA causes an unexpected Mg diffusion. Thus, both annealing processes resulted in a much lower Mg concentration in the GaN matrix than the Mg dose. In this study, the effect of a sequential N I/I for *p*-type Mg-implanted GaN was investigated by the correlative cathodoluminescence (CL), transfer length method (TLM), scanning transmission electron microscopy (STEM), and atom probe tomography (APT) analyses. APT results have revealed that the sequential N I/I can successfully maintain the Mg concentration in the GaN matrix in the higher range of 10^{18} cm^{-3} or more. Our investigation suggests that sequential N I/I is a promising technique to maintain the Mg concentration higher and improve the *p*-type activation efficiency.

Introduction

Gallium nitride (GaN) has attracted by its capability for the next-generation devices in high-power switching applications [1-2]. Owing to the recent improvements in the GaN crystal growth technique [3], the demonstrations of vertical-type GaN devices have been reported [4-12]. For application in high-power switching, the metal oxide semiconductor (MOS) gate driving is desired, thus, several studies of MOS field-effect transistors (MOSFETs) in both lateral and vertical structures were reported [13-22]. Considering practicality and reliability, it is essential to precisely control area selective conduction types by ion implantation (I/I) technique. However, forming *p*-type GaN by Mg I/I is still a critical problem. The Mg I/I unavoidably introduce defects into GaN, resulting in low activation efficiency compared with Mg doping via epitaxial growth [23]. A high-temperature post-implantation annealing is commonly carried out to recover these defects and activate Mg atoms [24], however, it results in an inefficient *p*-type activation due to the formation of defects [23-28]. Recently, the ultra-high-pressure annealing (UHPA) technique substantially improved the Mg activation efficiency [28-37]. However, a significant Mg diffusion is reported as one of the features of the UHPA [28-37]. An efficient *p*-type activation with high Mg concentration is required for ohmic contact formation to realize the GaN-based MOSFETs [22], however, both annealing techniques drastically decrease Mg concentration in the GaN matrix due to Mg clustering (conventional annealing) or Mg diffusion (UHPA) [26-28]. To overcome these problems, the sequential N I/I technique has been recently reported [38-42]. In this work, the effect of a sequential N I/I technique on shallow Mg I/I layer was studied by using correlative analysis techniques; secondary ion mass spectrometry (SIMS), cathodoluminescence (CL), transfer length method (TLM), scanning transmission electron microscopy (STEM), and atom probe tomography (APT) analyses. These results have clarified how the sequential N I/I technique affects the formation of defects, Mg distribution, and *p*-type activation.

Experimental methods

A 4 μm thick homoepitaxial *n*-GaN layer was grown by metal-organic chemical vapor deposition (MOCVD) on a [0001] oriented free-standing GaN substrate. The GaN substrate was prepared by the standard hydride vapor phase epitaxy (HVPE) technique [43]. Mg and N ions were shallowly implanted on the *n*-GaN epitaxial layer in 7 dgrees with twist 15 degrees at room temperature with different doses at 25 keV for Mg and 15 keV for N. Four dose levels ranging from 0.9×10^{14} to 5.4×10^{14} cm^{-2} were designed. Samples with different dose levels are referred to as Mg(n)+N(m), here, “n” and “m” are numbers. "1" represents a dose of 0.9×10^{14} cm^{-2}, "2" is twice that amount, 1.8×10^{14} cm^{-2}, "3" is 3.6×10^{14} cm^{-2}, and "4" is 5.4×10^{14} cm^{-2}. For example, the sample name "Mg(2)+N(4)" indicates a

dose of 1.8×10^{14} cm^{-2} for Mg and 5.4×10^{14} cm^{-2} for N. **Table 1** shows the sequential Mg and N I/I GaN samples used in this study. Four samples named as Mg(1)+N(1), Mg(2)+N(2), Mg(2)+N(4) and Mg(4)+N(4) were selected from a variety of combinations. Thereafter, conventional post-implantation annealing under an N_2 atmosphere at 1573 K for 5 min was performed with a 300 nm AlN encapsulation cap by a sputtering method to prevent GaN dissociation. Finally, the AlN cap was chemically removed. Details can be found at Kumar *et al.* [26].

Mg concentrations as a function of depth were analyzed by SIMS using O_2^+ ions as primary ions with a beam energy of 5 keV. The CL measurements were carried out by a *HORIBA* MP32 CL system attached to a *Hitachi* SU6600 field emission scanning electron microscope at 2 keV with a specimen temperature of 80 K. Considering the penetration depth of the electron beam, the CL result with 2 keV corresponds to the emission from ~40 nm depth. In addition, an angle cutting cross-sectional sample preparation method was carried out at 3 keV to reveal the depth distribution of the donor-acceptor-pair (DAP) emissions [44]. TLM measurement was done to determine the I-V characteristics. Ni (50 nm) / Au (150 nm) were used as an anode electrode, and N_2 gas annealing was performed at 723K for 4 minutes [22]. STEM and APT techniques were applied for the microstructural investigations. STEM observations were carried out by using a *Thermo Fisher Scientific* Titan G2 80-200. APT analyses were carried out using a *CAMECA* LEAP 5000XS. Both STEM and APT specimens were prepared by using a focused ion beam (FIB) with a scanning electron microscopy (SEM) system, *Thermo Fisher Scientific* Helios 5UX, with a 2 keV final cleaning [45, 46]. APT measurements were carried out with 10 fJ UV laser pulsing at a specimen temperature of 30 K. It should be noted that 1×10^{19} cm^{-3} corresponds to 0.0114 at% in APT, and the APT detection limit of Mg with this measuring condition is a higher range of 10^{17} cm^{-3}.

Samples	Mg dose (cm^{-2})	N dose (cm^{-2})	SIMS & APT			TLM		CL	
			$[Mg_{SIMS}]$ (cm^{-3})	$[Mg_{matrix}]$ (cm^{-3})	Mg clusters (nm^{-3})	Rs ($\Omega/\square$)	ρc (Ωcm^2)	DAP (count/s)	GL (count/s)
Mg(1)+N(1)	0.9×10^{14}	0.9×10^{14}	7.0×10^{18}	4.9×10^{18}	0.8×10^{-3}	3.0×10^{5}	0.20	72.8	29.0
Mg(2)+N(2)	1.8×10^{14}	1.8×10^{14}	2.0×10^{19}	8.6×10^{18}	0.7×10^{-3}	1.5×10^{5}	0.0076	119.3	6.6
Mg(2)+N(4)	1.8×10^{14}	5.4×10^{14}	3.0×10^{19}	8.0×10^{18}	1.5×10^{-3}	N/A	N/A	1.8	2.5
Mg(4)+N(4)	5.4×10^{14}	5.4×10^{14}	9.0×10^{19}	1.6×10^{19}	2.0×10^{-3}	2.7×10^{5}	0.37	26.1	4.8

Table 1. Sequential Mg and N I/I GaN samples used in this study. The implantation doses of Mg and N, the concentrations of Mg and cluster extracted from SIMS and APT measurements, the sheet resistivity R_s and contact resistance ρ_c based on TLM, and the CL intensity of donor-acceptor pair (DAP) and green luminescence (GL) at ~40 nm

depth are listed. (N/A: not available)

Results and Discussion

Figure 1 shows the Mg concentration profiles measured by SIMS. **Fig. 1(a)** shows the profile down to a depth of 800 nm, and **Fig. 1(b)** shows magnified profiles near the sample surfaces. It should be noted that the profiles below 35 nm were intentionally excluded to rule out uncertainties such as surface roughness, and as-implanted Mg and N profiles is drawn as dotted-lines by the stopping and range of ions in matter (SRIM) simulation in the case of 1.8×10^{14} cm^{-2} dose. At the depth of 40 nm, the Mg concentration measured by SIMS (hereafter refered to as [Mg_{SIMS}]) was maintained at approximately 7.0×10^{18} cm^{-3} for the sample Mg(1)+N(1), 2.0×10^{19} cm^{-3} for Mg(2)+N(2), 3.0×10^{19} cm^{-3} for Mg(2)+N(4), and 9.0×10^{19} cm^{-3} for Mg(4)+N(4). The [Mg_{SIMS}] values of Mg(2)+N(2) and Mg(2)+N(4) were almost identical. However, the magnitude of Mg diffusion in the depth direction varied depending on the dose conditions. The Mg diffusion was inhibited by increasing the N dose. From **Fig. 1(a)**, it can be found that the diffusion depth of Mg was in the order of Mg(1) +N(1) (~600 nm) > Mg(2)+N(2) (~400 nm) > Mg(4)+N(4) (~300 nm) > Mg(2)+N(4) based on Fick's law [47, 48]. In the case of the Mg(2)+N(4), the diffusion of Mg is less obvious compared with the other samples. The effectiveness in suppressing the Mg diffusion by the sequential N I/I (called "vacancy-guided Mg redistribution technique") was reported by previous studies [38, 40].

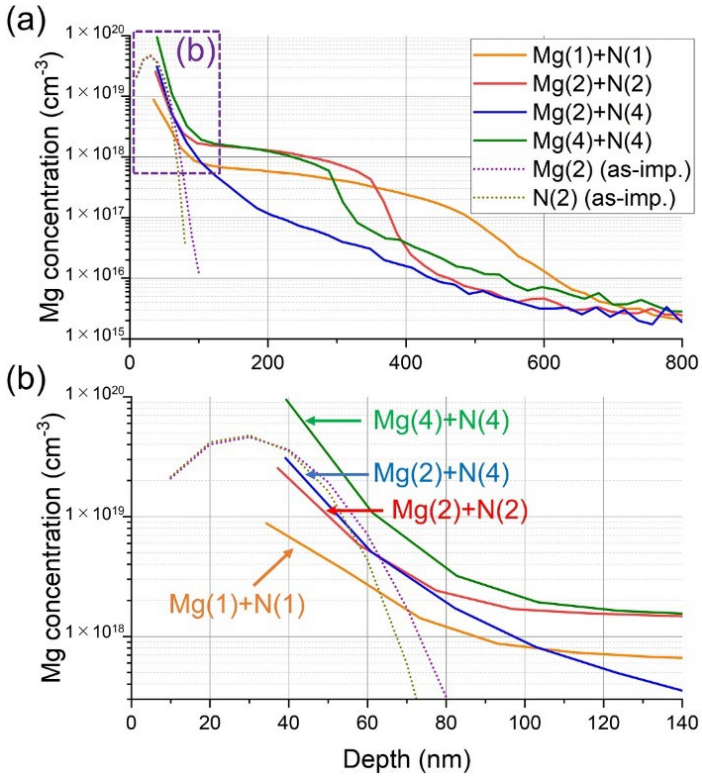

Figure 1. Mg concentration profiles measured by SIMS. (a) Mg profiles up to 800 nm depth, and (b) magnified profiles

near the sample surfaces indicated purple box in (a). As-implanted Mg and N profiles is drawn as dotted-lines by the stopping and range of ions in matter (SRIM) simulation in the case of 1.8×10^{14} cm^{-2} dose.

Figure 2(a-d) shows the angle-cutting cross-sectional CL images of the donor-acceptor-pair (DAP) emission (2.7~3.3 eV) of the four samples. It was found that the DAP luminescence depth became shallower as the N dose increased. Since DAP emission is associated with Mg activation [27, 28], the depth of DAP luminescence was in good agreement with the Mg diffusion observed by SIMS. **Fig. 2(e)** shows the CL spectra of green luminescence (GL) (2.1~2.5 eV) and DAP emission (2.7~3.3 eV), which were taken at an accelerating voltage of 2 keV, corresponding to the electron range of ~ 40 nm depth. When the dose was Mg(1)+N(1), the CL intensity of GL remained strong. On the other hand, the Mg(2)+N(2) sample showed a weakened GL emission and an enhanced DAP emission. The GL emission was considered to be associated with the presence of N vacancy-type defects (V_N) [38-40, 49, 50]; therefore, the CL results suggest that it is effective in suppressing the number of V_N by the sequential N I/I technique. However, if the doses of Mg or N were further increased, the DAP intensity decreased, suggesting that a higher N dose may induce non-radiative centers.

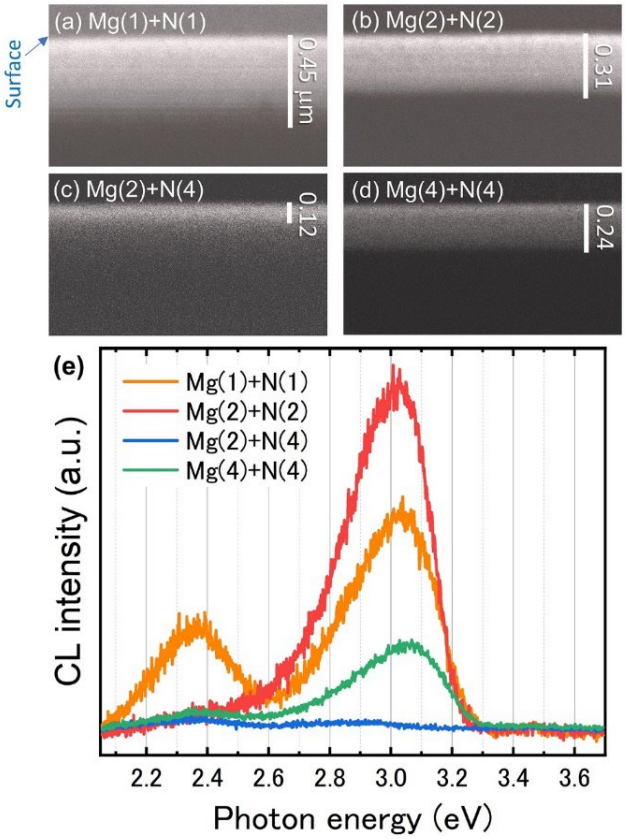

Figure 2. Angle-cutting cross-sectional CL images of the donor-acceptor-pair (DAP) emission (2.7~3.3 eV) of (a) Mg(1)+N(1), (b) Mg(2)+N(2), (c) Mg(2)+N(4), and (d) Mg(4)+N(4) samples. Note that the tilt correction in the depth direction was applied for CL images. (e) The CL intensity of the green band (2.1~2.5 eV) and the DAP emission (2.7~3.3 eV) at 2 keV.

Figure 3 shows the results of the TLM measurement. The values of sheet resistance R_s (Ω/□) and contact resistance ρ_c (Ωcm^2) are written in the graphs. Since Schottky-like curves were observed in all the samples, the values were calculated by using a method to evaluate the nonlinear curves reported by Piotrzkowski *et al.* [51]. The Mg(2)+N(2) sample has the best properties, the lowest R_s and ρ_c (**Fig. 3(b)**), and the others have worse properties. Tanaka *et al.* reported the only Mg I/I sample showing almost no current flow [22], therefore, it can be concluded that the sequential N I/I technique has improved the *p*-type activation. However, the properties are again degraded if the N dose becomes higher than Mg(2)+N(2) (**Fig. 3(c) and (d)**). Almost no current flow was observed in the Mg(2)+N(4). The samples with Mg(2)+N(1), Mg(2)+N(3), Mg(3)+N(3) conditions also show worse properties compared with Mg(2)+N(2) (see **Suppl. Fig. 1**). In this study, the Mg(2)+N(2) was somehow in the sweet spot. The results of TLM and CL measurements agree with each other, that is, the Mg(2)+N(2) shows the best properties in R_s and ρ_c (TLM), the highest DAP, and the lowest GL emissions (CL). Also, the Mg(2)+N(4) shows almost no current flow in TLM, and no DAP emissions by CL analysis.

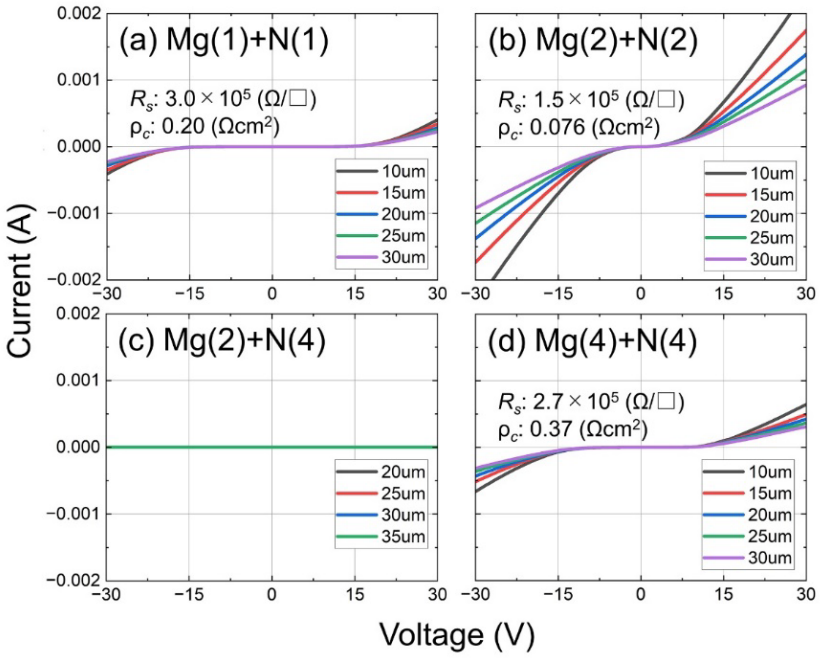

Figure 3. The results of the TLM measurement of shallow Mg and N I/I samples. (a) Mg(1)+N(1), (b) Mg(2)+N(2), (c) Mg(2)+N(4), and (d) Mg(4)+N(4).

To reveal the relationship between the properties and the microstructures of samples, STEM and APT were applied. **Figure 4** shows the cross-sectional low-angle annular dark field (LAADF)-STEM images. Distortion caused by the vacancy clusters, or the Mg clustering in the GaN gives a bright contrast in the LAADF-STEM image as reported previously [26-29, 40, 41]. The low-magnification

images are shown in **Fig. 4(a-d)**, and a large number of tiny bright dots are observed in all the samples. The typical defect in higher magnification is shown in **Fig. 4(e)**. These defects are the extrinsic stacking fault on the *c*-plane highlighted with pink-colored marks as reported previously [26, 29, 33]. From the low magnification images, the number densities of these defects seem to be increasing with the increase of N dose.

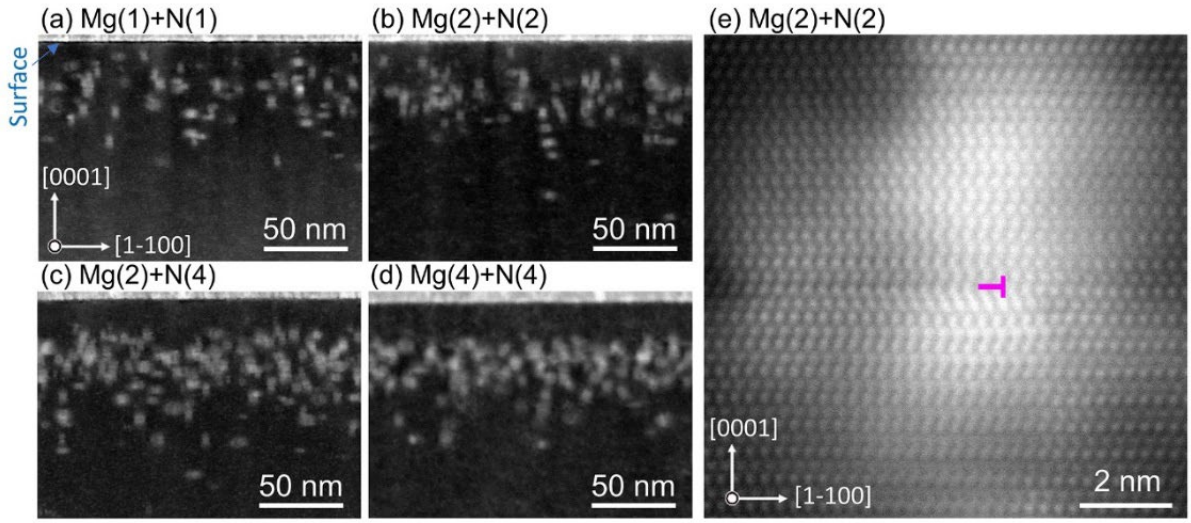

Figure 4. (a-d) Low-magnification cross-sectional LAADF-STEM images. (e) Typical defect in higher magnification. Pink-colored marks indicates the extrinsic stacking fault on the c-plane.

Figure 5 shows the results obtained by APT. To avoid complications, the three-dimensional Mg distributions of only the Mg(2)+N(2) sample are shown in **Fig. 5(a) and (b). Fig. 5(a)** shows the Mg distribution up to ~100 nm depth, and one of the typical Mg clusters is shown in **Fig. 5(b)**. Disk-shaped Mg clusters on the *c*-plane were formed in all the samples. The extrinsic stacking fault on the *c*-plane observed by STEM corresponds to these disk-shaped Mg clusters. To compare with the SIMS results, the Mg concentrations in the GaN matrix (hereafter, refer to [Mg_{matrix}]) at 40 nm depth were calculated by excluding Mg clusters from APT data. A threshold of 0.3 at% Mg was used here. The results of [Mg_{matrix}] are as below; ~4.9×10^{18} cm^{-3} (Mg(1)+N(1)), ~8.6×10^{18} cm^{-3} (Mg(2) +N(2)), ~8.0×10^{18} cm^{-3} (Mg(2)+N(4)), and ~1.6×10^{19} cm-3 (Mg(4)+N(4)) as summarized in **Fig. 5(c)**. APT analysis eveals that the increase in Mg dose keeps the [Mg_{matrix}] increasing. Both the [Mg_{SIMS}] and the [Mg_{matrix}] are in the order of the Mg doses. At the same time, the increase of Mg and N I/I doses strongly enhances the formation of Mg clusters as the calculated number densities of Mg clusters shown in **Fig. 5(d)**. Between Mg(1)+N(1) and Mg(2)+N(2) samples, there is no significant difference in the number density (0.8×10^{-3} nm^{-3} for Mg(1)+N(1), and 0.7×10^{-3} nm^{-3} for Mg(2)+N(2)). On the other hand, the number density increases to 1.5×10^{-3} nm^{-3} for Mg(2)+N(4), and 2.0×10^{-3} nm^{-3} for Mg(4)+N(4).

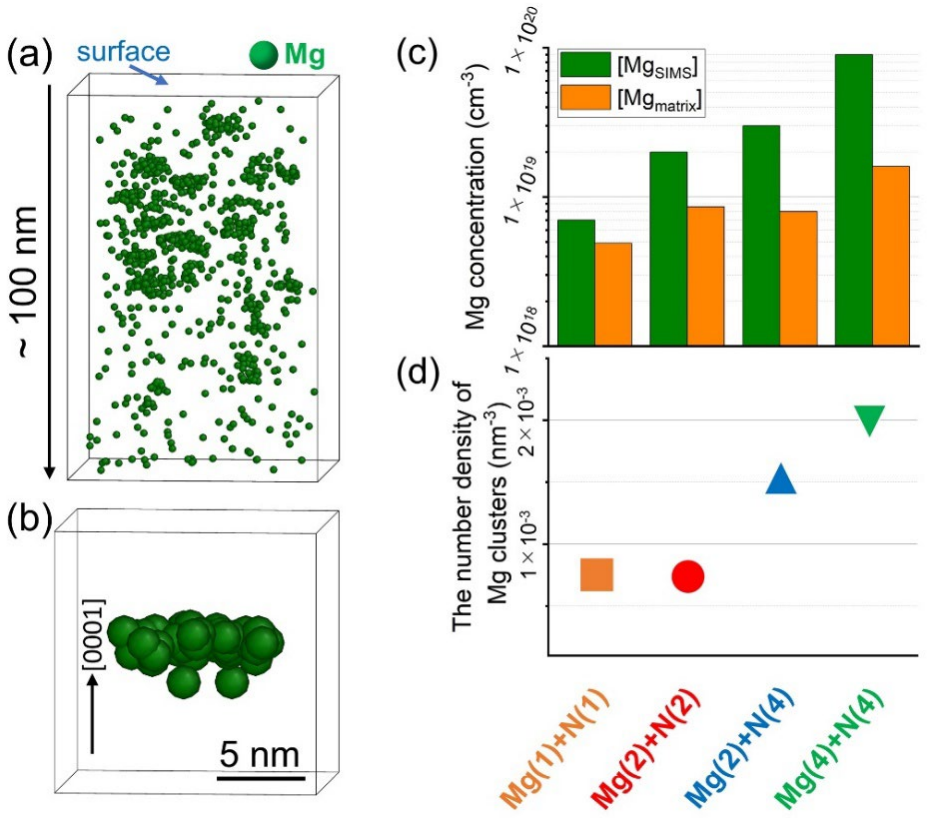

Figure 5. (a) Three-dimensional Mg atoms distributions up to ~100 nm depth, and (b) typical Mg clusters. (c) Calculated Mg concentrations of [Mg_{SIMS}] and [Mg_{matrix}] from SIMS and APT results at ~40 nm depth. (d) The number density of Mg clusters calculated from 30 to 50 nm depth.

Table 1 is a summary of SIMS, APT, TLM, and CL data taken inside the I/I layer with a depth of ~ 40 nm, including the Mg concentrations measured by SIMS and APT, the number density of Mg clusters, the sheet resistivity R_s and contact resistance ρ_c, as well as the CL intensity of donor-acceptor pair (DAP) and green luminescence (GL). To discuss the effect of sequential N I/I, two types of comparison are made. One type of comparison is the effect of increasing Mg and N doses while maintaining the same ratio. Another comparison is the effect of increasing the N dose while keeping the Mg dose fixed at 1.8×10^{14} cm^{-2}.

For the comparison of samples with simultaneous increases in Mg and N doses (Mg(1)+N(1), Mg(2)+N(2), and Mg(4)+N(4)), the increase in Mg dose successfully made both [Mg_{SIMS}] and [Mg_{matrix}] higher. This result is consistent with the reports by Uedono *et al.* and Kano *et al.* that the trapping of implanted Mg ions in vacancies was enhanced by the sequential N I/I [40, 42]. There was no significant difference in the number density of Mg clusters between the Mg(1)+N(1) and Mg(2)+N(2) samples; whereas the [Mg_{matrix}] became higher in the Mg(2)+N(2) sample. On another hand, strong GL emission observed in the Mg(1)+N(1) sample indicated the presence of a high density

of V_N defects [38, 39, 41], whereas in the Mg(2)+N(2) sample, the intensity of GL emission was considerably reduced, suggesting that V_N defects were suppressed. We can conclude that the higher [Mg_{matrix}] and lower N vacancy-type defects in Mg(2)+N(2) are the main reasons for the improved electrical properties. However, the number density of Mg clusters in the Mg(4)+N(4) sample was more than twice that of the Mg(1)+N(1) and Mg(2)+N(2) samples. It has been reported the formation of Mg clusters strongly suppressed the DAP emissions associated with *p*-type activation [27, 28, 52]. Thus, the TLM property and DAP emissions of the Mg(4)+N(4) sample are considered to be degraded because of an increase in Mg-enriched defects.

In another comparison of samples where only the N dose increased (Mg(2)+N(2) and Mg(2)+N(4)), there was no significant difference in [Mg_{SIMS}] and [Mg_{matrix}] due to the same Mg dose. Nevertheless, the Mg(2)+N(4) sample showed almost no current flow in TLM and very weak DAP emission in CL. We have investigated a series of samples with the Mg dose fixed at 1.8×10^{14} cm^{-2} and N dose varied from 0.9×10^{14} (Mg(2)+N(1)), 1.8×10^{14} (Mg(2)+N(2)), 3.6×10^{14} (Mg(2)+N(3)) to 5.4×10^{14} cm^{-2} (Mg(4)+N(4)) (see **Suppl. Table 1**). In the Mg(2)+N(1) sample, DAP emission was strong; however, GL emission was also strong due to insufficient N I/I resulting in still high-density V_N defects; in the Mg(2)+N(3) and Mg(2)+N(4) samples, both DAP and GL emissions extremely decreased. Sakurai *et al.* reported that an excessive N I/I reduced the entire CL intensity, indicating an increase in the nonradiative recombination centers (NRCs) [39]. Uedono *et al.* reported that sequential N I/I increased not only the concentration of vacancy-type defects but also other types of defects such as dislocation loops, Mg clusters, and stacking faults [41]. Thus, the worst properties of TLM and CL of Mg(2) +N(4) sample are probably due to the introduction of numerous NRCs owing to excess N I/I [53]. This comparison strongly indicates that the Mg/N dose ratio changes the balance between the vacancy concentration and the size of vacancy clusters, the formation of stacking faults and Mg clusters.

Conclusions

In summary, it was revealed that the sequential N I/I dose technique has both positive and negative effects on *p*-type activation; the positive effect is to make [Mg_{matrix}] higher and to reduce V_N, and the negative effect is enhancing the formation of Mg clusters and the introduction of vacancies, resulting in suppressing the *p*-type activation efficiency. An insufficient N dose cannot suppress the V_N, resulting in strong GL emission; however, an excessive N I/I introduces numerous NRCs originating from vacancy-type defects, resulting in weak emission in entire CL spectra. Here, we can conclude that optimizing the I/I condition is a trade-off between the Mg concentration in the GaN matrix and the number density of these defects. Our investigations have clarified that the optimized sequential N I/I

condition enables the Mg concentration to maintain higher and improves the *p*-type activation efficiency.

Supplementary Material

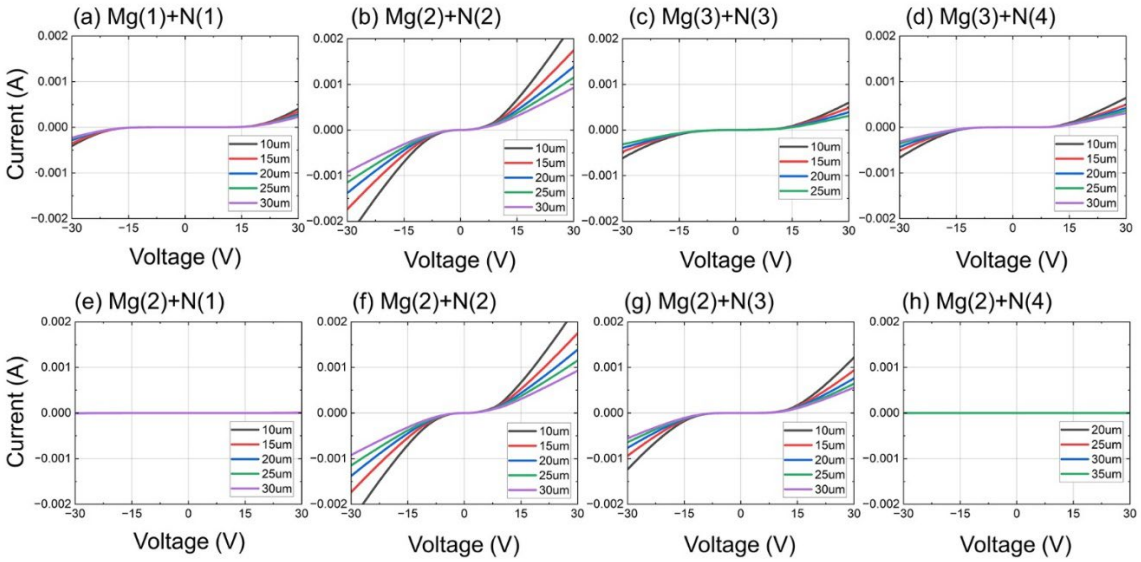

Suppl. Fig. 1. The results of the TLM measurement of shallow Mg and N I/I samples.

Sample	Mg dose (cm^{-2})	N dose (cm^{-2})	SIMS & APT			CL		
			$[Mg_{SIMS}]$ (cm^{-3})	$[Mg_{matrix}]$ (cm^{-3})	Mg cluster (nm^{-3})	DAP Intensity	GL Intensity	DAP/GL
Mg(1)+N(1)	0.9×10^{14}	0.9×10^{14}	7.0×10^{18}	4.9×10^{18}	0.8×10^{-3}	72.8	29.0	2.5
Mg(2)+N(2)	1.8×10^{14}	1.8×10^{14}	2.0×10^{19}	8.6×10^{18}	0.7×10^{-3}	119.3	6.6	18.1
Mg(3)+N(3)	3.6×10^{14}	3.6×10^{14}	5.0×10^{19}	9.0×10^{18}	1.2×10^{-3}	60.4	7.9	7.6
Mg(4)+N(4)	5.4×10^{14}	5.4×10^{14}	9.0×10^{19}	1.6×10^{19}	2.0×10^{-3}	26.1	4.8	5.4

Sample	Mg dose (cm^{-2})	N dose (cm^{-2})	SIMS & APT			CL		
			$[Mg_{SIMS}]$ (cm^{-3})	$[Mg_{matrix}]$ (cm^{-3})	Mg cluster (nm^{-3})	DAP Intensity	GL Intensity	DAP/GL
Mg(2)+N(1)	1.8×10^{14}	0.9×10^{14}	1.9×10^{19}	5.3×10^{18}	0.3×10^{-3}	232.5	149.7	1.5
Mg(2)+N(2)	1.8×10^{14}	1.8×10^{14}	2.0×10^{19}	8.6×10^{18}	0.7×10^{-3}	119.3	6.6	18.1
Mg(2)+N(3)	1.8×10^{14}	3.6×10^{14}	2.9×10^{19}	8.5×10^{18}	1.0×10^{-3}	5.3	1.5	3.5
Mg(2)+N(4)	1.8×10^{14}	5.4×10^{14}	3.0×10^{19}	8.0×10^{18}	1.5×10^{-3}	1.8	2.5	0.7

Suppl. Table 1. Sequential Mg and N I/I GaN samples used in this study. The implantation doses of Mg and N, the concentrations of Mg and cluster extracted from SIMS and APT measurements, and the CL intensity of donor-acceptor pair (DAP) and green luminescence (GL) at ~40 nm depth are listed.

Acknowledgments

The support for this research was provided by the Ministry of Education, Culture, Sports, Science and Technology (MEXT), Japan, through its Program for Creation of Innovative Core Technology for Power Electronics Grant No. JPJ009777. The authors thank Kyoko Suzuki for her technical support of STEM/APT analyses.

References

1. T.P. Chow and R. Tyagi, IEEE Trans. Electron Devices **41**, 1481 (1994). https://doi.org/10.1109/16.297751
2. T. J. Flack, B. N. Pushpakaran, and S. B. Bayne, J. Electron. Mater. **45**, 2673 (2016). https://doi.org/10.1007/s11664-016-4435-3
3. H. Amano, Jpn. J. Appl. Phys. **52**, 050001 (2013). https://doi.org/10.7567/JJAP.52.050001
4. Y. Saitoh, K. Sumiyoshi, M. Okada, T. Horii, T. Miyazaki, H. Shiomi, M. Ueno, K. Katayama, M. Kiyama and T. Nakamura, Appl. Phys. Express **3**, 081001 (2010). https://doi.org/10.1143/APEX.3.081001
5. K. Nomoto, Y. Hatakeyama, H. Katayose, N. Kaneda, T. Mishima, T. Nakamura, Phys. Status Solidi A **208**, 1535 (2011). https://doi.org/10.1002/pssa.201000976
6. Y. Hatakeyama, K. Nomoto, N. Kaneda, T. Kawano, T. Mishima and T. Nakamura, IEEE Electron Device Lett. **32**, 1674 (2011). https://doi.org/10.1109/LED.2011.2167125
7. I.C. Kizilyalli, A.P. Edwards, H. Nie, D. Disney and D. Bour, IEEE Trans. Electron Devices **60**, 3067 (2013). https://doi.org/10.1109/TED.2013.2266664
8. T. Oka, Y. Ueno, T. Ina and K. Hasegawa, Appl. Phys. Express **7**, 021002 (2014). https://doi.org/10.7567/APEX.7.021002
9. I.C. Kizilyalli, A.P. Edwards, H. Nie, D. Bour, T. Prunty and D. Disney, IEEE Electron Device Lett. **35**, 247 (2014). https://doi.org/10.1109/LED.2013.2294175
10. T. Oka, T. Ina, Y. Ueno and J. Nishii, Appl. Phys. Express **8**, 054101 (2015). https://doi.org/10.7567/APEX.8.054101
11. H. Ohta, N. Kaneda, F. Horikiri, Y. Narita, T. Yoshida, T. Mishima and T. Nakamura, IEEE Electron Device Lett. **36**, 1180 (2015). https://doi.org/10.1109/LED.2015.2478907
12. K. Nomoto, B. Song, Z. Hu, M. Zhu, M. Qi, N. Kaneda, T. Mishima, T. Nakamura, D. Jena and H.G. Xing, IEEE Electron Device Lett. **37**, 161 (2016). https://doi.org/10.1109/LED.2015.2506638
13. Y. Irokawa, Y. Nakano, M. Ishiko, T. Kachi, J. Kim, F. Ren, B.P. Gila, A. H. Onstine, C. R. Abernathy, S. J. Pearton, C.-C. Pan, G.-T. Chen, J.-I. Chyi, Appl. Phys. Lett. **84**, 2919–2921 (2004).

https://doi.org/10.1063/1.1704876

14. W. Huang, T. Khan and T.P. Chow, IEEE Electron Device Lett. **27**, 796 (2006). https://doi.org/10.1109/LED.2006.883054
15. H. Otake, S. Egami, H. Ohta, Y. Nanishi and H. Takasu, Jpn. J. Appl. Phys. **46**, L599 (2007). https://doi.org/10.1143/JJAP.46.L599
16. M. Kodama, M. Sugimoto, E. Hayashi, N. Soejima, O. Ishiguro, M. Kanechika, K. Itoh, H. Ueda, T. Uesugi and T. Kachi, Appl. Phys. Express **1**, 021104 (2008). https://doi.org/10.1143/APEX.1.021104
17. H. Otake, K. Chikamatsu, A. Yamaguchi, T. Fujishima and H. Ohta, Appl. Phys. Express **1**, 011105 (2008). https://doi.org/10.1143/APEX.1.011105
18. Y. Niiyama, S. Ootomo, J. Li, T. Nomura, S. Kato and T.P. Chow, Semicond. Sci. Technol. **25**, 125006 (2010). https://doi.org/10.1088/0268-1242/25/12/125006
19. S. Takashima, K. Ueno, H. Matsuyama, T. Inamoto, M. Edo, T. Takahashi, M. Shimizu and K. Nakagawa, Appl. Phys. Express **10**, 121004 (2017). https://doi.org/10.7567/APEX.10.121004
20. R. Tanaka, S. Takashima, K. Ueno, H. Matsuyama and M. Edo, Jpn. J. Appl. Phys. **59**, SGGD02 (2020). https://doi.org/10.7567/1347-4065/ab6347
21. R. Tanaka, S. Takashima, K. Ueno, H. Matsuyama, M. Edo and K. Nakagawa, Appl. Phys. Express **12**, 054001 (2019). https://doi.org/10.7567/1882-0786/ab0c2c
22. R. Tanaka, S. Takashima, K. Ueno, M. Horita, J. Suda, J. Uzuhashi, T. Ohkubo, M. Edo, 2023 21st International Workshop on Junction Technology (IWJT). https://doi.org/10.23919/IWJT59028.2023.10175173
23. T. Narita, T. Kachi, K. Kataoka, and T. Uesugi, Appl. Phys. Express **10**, 016501 (2017). https://doi.org/10.7567/APEX.10.016501
24. T. Niwa, T. Fujii, and T. Oka, Appl. Phys. Express **10**, 091002 (2017). https://doi.org/10.7567/APEX.10.091002
25. A. Uedono, S. Takashima, M. Edo, K. Ueno, H. Matsuyama, W. Egger, T. Koschine, C. Hugenschmidt, M. Dickmann, K. Kojima, S. F. Chichibu, and S. Ishibashi, Phys. Status Solidi B **255**, 1700521 (2018). https://doi.org/10.1002/pssb.201700521
26. A. Kumar, J. Uzuhashi, T. Ohkubo, R. Tanaka, S. Takashima, M. Edo, and K. Hono, J. Appl. Phys. **126**, 235704 (2019). https://doi.org/10.1063/1.5132345
27. A. Kumar, W. Yi, J. Uzuhashi, T. Ohkubo, J. Chen, T. Sekiguchi, R. Tanaka, S. Takashima, M. Edo, K. Hono, J. Appl. Phys. **128**, 065701 (2020). https://doi.org/10.1063/5.0142766
28. J. Uzuhashi, J. Chen, A. Kumar, W. Yi, T. Ohkubo, R. Tanaka, S. Takashima, M. Edo, K. Sierakowski, M. Bockowski, H. Sakurai, T. Kachi, T. Sekiguchi, and K. Hono, J. Appl. Phys. **131**,

185701 (2022). https://doi.org/10.1063/5.0087248

29. E. Kano, K. Kataoka, J. Uzuhashi, K. Chokawa, H. Sakurai, A. Uedono, T. Narita, K. Sierakowski, M. Bockowski, R. Otsuki, K. Kobayashi, Y. Ito, M. Nagao, T. Ohkubo, K. Hono, J. Suda, T. Kachi, and N. Ikarashi, J. Appl. Phys. **132**, 065703 (2022). https://doi.org/10.1063/5.0097866
30. H. Sakurai, M. Omori, S. Yamada, Y. Furukawa, H. Suzuki, T. Narita, K. Kataoka, M. Horita, M. Bockowski, J. Suda, and T. Kachi, Appl. Phys. Lett. **115**, 142104 (2019). https://doi.org/10.1063/1.5116866
31. K. Sierakowski, R. Jakiela, B. Lucznik, P. Kwiatkowski, M. Iwinska, M. Turek, H. Sakurai, T. Kachi and M. Bockowski, Electronics **9**, 1380 (2020). https://doi.org/10.3390/electronics9091380
32. T. Nakashima, E. Kano, K. Kataoka, S. Arai, H. Sakurai, T. Narita, K. Sierakowski, M. Bockowski, M. Nagao, J. Suda, Appl. Phys. Express **14** 011005 (2021). https://doi.org/10.35848/1882-0786/abd308
33. K. Iwata, H. Sakurai, S. Arai, T. Nakashima, T. Narita, K. Kataoka, M. Bockowski, M. Nagao, J. Suda, T. Kachi, and N. Ikarashi, J. Appl. Phys. **127**, 105106 (2020). https://doi.org/10.1063/1.5140410
34. K. Sumida, K. Hirukawa, H. Sakurai, K. Sierakowski, M. Horita, M. Bockowski, T. Kachi and J. Suda, Appl. Phys. Express **14**, 121004 (2021). https://doi.org/10.35848/1882-0786/ac39b0
35. A. Uedono, H. Sakurai, T. Narita, K. Sierakowski, M. Bockowski, J. Suda, S. Ishibashi, S.F. Chichibu & T. Kachi, Sci. Rep. **10**, 17349 (2020). https://doi.org/10.1038/s41598-020-74362-9
36. T. Narita, H. Sakurai, M. Bockowski, K. Kataoka, J. Suda and T. Kachi, Appl. Phys. Express **12,** 111005 (2019). https://doi.org/10.1002/10.7567/1882-0786/ab4934
37. H. Sakurai, T. Narita, M. Omori, S. Yamada, A. Koura, M. Iwinska, K. Kataoka, M. Horita, N. Ikarashi, M. Bockowski, J. Suda and T. Kachi, Appl. Phys. Express **13**, 086501 (2020). https://doi.org/10.35848/1882-0786/aba64b
38. K. Shima, R. Tanaka, S. Takashima, K. Ueno, M. Edo, K. Kojima, A. Uedono, S. Ishibashi, S. F. Chichibu, Appl. Phys. Lett. **119**, 182106 (2021). https://doi.org/10.1063/5.0066347
39. Hideki Sakurai, Tetsuo Narita, Keita Kataoka, Kazufumi Hirukawa, Kensuke Sumida, Shinji Yamada, Kacper Sierakowski, Masahiro Horita, Nobuyuki Ikarashi, Michal Bockowski, Jun Suda and Tetsu Kachi, Appl. Phys. Express **14**, 111001 (2021). https://doi.org/10.35848/1882-0786/ac2ae7
40. A. Uedono, H. Sakurai, J. Uzuhashi, T. Narita, K. Sierakowski, S. Ishibashi, S.F. Chichibu, M. Bockowski, J. Suda, T. Ohkubo, N. Ikarashi, K. Hono, and T. Kachi, Phys. Status Solidi B **259**, 2200183 (2022). https://doi.org/10.1002/pssb.202200183
41. A. Uedono, R. Tanaka, S. Takashima, K. Ueno, M. Edo, K. Shima, S.F. Chichibu, J. Uzuhashi, T.

Ohkubo, S. Ishibashi, K. Sierakowski, and M. Bockowski, Status Solidi **261**, 2400060 (2024). https://doi.org/10.1002/pssb.202400060

42. Emi Kano, Jun Uzuhashi, Koki Kobayashi, Kosuke Ishikawa, Kyosuke Sawabe, Tetsuo Narita, Kacper Sierakowski, Michal Bockowski, Tadakatsu Ohkubo, Tetsu Kachi, Nobuyuki Ikarashi, Phys. Status Solidi Rapid Res. Lett. **18**, 2400074 (2024). https://doi.org/10.1002/pssr.202400074
43. K. Naniwae, S. Itoh, H. Amano, K. Itoh, K. Hiramatsu, I. Akasaki, Journal of Crystal Growth **99**, 381-384 (1990). https://doi.org/10.1016/0022-0248(90)90548-Y
44. J. Chen, W. Yi, T. Kimura, S. Takashima, M. Edo, and T. Sekiguchi, Appl. Phys. Express **12**, 051010 (2019). https://doi.org/10.7567/1882-0786/ab14cb
45. T. Sato, K. Nakano, H. Matsumoto, S. Torikawa, I. Nakatani, M. Kiyohara and T. Isshiki, High quality lamella preparation of gallium nitride compound semiconductor using Triple Beam system, J. Phys.: Conf. Ser. **902**, 012019 (2017). https://doi.org/10.1088/1742-6596/902/1/012019
46. J. Uzuhashi and T. Ohkubo, Ultramicroscopy **262**, 113980 (2024). https://doi.org/10.1016/j.ultramic.2024.113980
47. T. Narita, A. Uedono, T. Kachi, Phys. Status Solidi B, 259: 2200235 (2022). https://doi.org/10.1002/pssb.202200235
48. K. Sierakowski, P. Jaroszynski, R. Jakiela, M. Fijalkowski, T. Sochacki, M. Iwinska, M. Turek, K. Lorenz, M. Bockowski, Materials Science in Semiconductor Processing 171, 108022 (2024). https://doi.org/10.1016/j.mssp.2023.108022
49. M. A. Reshchikov, D. O. Demchenko, J. D. McNamara, S. Fernández-Garrido, and R. Calarco, Phys. Rev. B **90**, 035207 (2014).
50. K. Kojima, S. Takashima, M. Edo, K. Ueno, M. Shimizu, T. Takahashi, S. Ishibashi, A. Uedono and S. F. Chichibu, Appl. Phys. Express **10**, 061002 (2017). https://doi.org/10.7567/APEX.10.061002
51. R. Piotrzkowski; E. Litwin-Staszewska; Sz. Grzanka, Appl. Phys. Lett. **99**, 052101 (2011). https://doi.org/10.1063/1.3619813
52. S. Khromov, D. Gregorius, R. Schiller, J. Lösch, M. Wahl, M. Kopnarski, H. Amano, B. Monemar, L. Hultman, and G. Pozina, Nanotechnology **25**, 275701 (2014). https://doi.org/10.1088/0957-4484/25/27/275701
53. S. F.Chichibu, A.Uedono, K.Kojima, H.Ikeda, K.Fujito, S.Takashima, M. Edo, K. Ueno and S. Ishibashi, J. Appl. Phys. **123**, 161413 (2018). https://doi.org/10.1063/1.5012994